

# NMMA: A nuclear-physics and multi-messenger astrophysics framework to analyze binary neutron star mergers

Peter T. H. Pang<sup>1,2</sup>, Tim Dietrich<sup>3,4</sup>, Michael W. Coughlin<sup>5</sup>, Mattia Bulla<sup>6</sup>, Ingo Tews<sup>7</sup>, Mouza Almualla<sup>8</sup>, Tyler Barna<sup>5</sup>, Weizmann Kiendrebeogo<sup>9,10</sup>, Nina Kunert<sup>3</sup>, Gargi Mansingh<sup>5,11</sup>, Brandon Reed<sup>5,12</sup>, Niharika Sravan<sup>13</sup>, Andrew Toivonen<sup>5</sup>, Sarah Antier<sup>10</sup>, Robert O. VandenBerg<sup>5</sup>, Jack Heinzel<sup>14</sup>, Vsevolod Nedora<sup>4</sup>, Pouyan Salehi<sup>3</sup>, Ritwik Sharma<sup>15</sup>, Rahul Somasundaram<sup>16</sup>, Chris Van Den Broeck<sup>1,2</sup>

<sup>1</sup>Nikhef, Science Park 105, 1098 XG Amsterdam, The Netherlands <sup>2</sup>Institute for Gravitational and Subatomic Physics (GRASP), Utrecht University, Princetonplein 1, 3584 CC Utrecht, The Netherlands <sup>3</sup>Institut für Physik und Astronomie, Universität Potsdam, Haus 28, Karl-Liebknecht-Str. 24/25, 14476, Potsdam, Germany <sup>4</sup>Max Planck Institute for Gravitational Physics (Albert Einstein Institute), Am Mühlenberg 1, Potsdam 14476, Germany <sup>5</sup>School of Physics and Astronomy, University of Minnesota, Minneapolis, Minnesota 55455, USA <sup>6</sup>The Oskar Klein Centre, Department of Astronomy, Stockholm University, AlbaNova, SE-106 91 Stockholm, Sweden <sup>7</sup>Theoretical Division, Los Alamos National Laboratory, Los Alamos, NM 87545, USA <sup>8</sup>Department of Physics, American University of Sharjah, PO Box 26666, Sharjah, UAE <sup>9</sup>Laboratoire de Physique et de Chimie de l'Environnement, Université Joseph KI-ZERBO, Ouagadougou, Burkina Faso <sup>10</sup>Artemis, Université Côte d'Azur, Observatoire Côte d'Azur, CNRS, CS 34229, F-06304 Nice Cedex 4, France <sup>11</sup>Department of Physics, American University, Washington, DC 20016, USA. <sup>12</sup>Department of Physics and Astronomy, University of Minnesota – Duluth, Duluth, MN 55812 <sup>13</sup>Division of Physics, Mathematics, and Astronomy, California Institute of Technology, Pasadena, CA 91125, USA <sup>14</sup>Department of Physics, Massachusetts Institute of Technology, 77 Massachusetts Ave, Cambridge, MA 02139, USA. <sup>15</sup>Department of Physics, Deshbandhu College, University of Delhi, New Delhi, India. <sup>16</sup>Univ Lyon, Univ Claude Bernard Lyon 1, CNRS/IN2P3, IP2I Lyon, UMR 5822, F-69622, Villeurbanne, France

**The multi-messenger detection of the gravitational-wave signal GW170817, the corresponding kilonova AT2017gfo and the short gamma-ray burst GRB170817A, as well as the observed afterglow has delivered a scientific breakthrough. For an accurate interpretation of all these different messengers, one requires robust theoretical models that describe the emitted gravitational-wave, the electromagnetic emission, and dense matter reliably. In addition, one needs efficient and accurate computational tools to ensure a correct cross-correlation between the models and the observational data. For this purpose, we have developed the NMMA (Nuclear-physics and Multi-Messenger Astrophysics) framework. The code allows incorporation of nuclear-physics constraints at low densities as well as X-ray and radio observations of isolated neutron stars. It also enables us to classify electromagnetic observations, e.g., to distinguish between supernovae and kilonovae. In previous works, the NMMA code has allowed us to constrain the equation of state of supranuclear dense matter, to measure the Hubble constant, and to compare dense-matter physics probed in neutron-star mergers and in heavy-ion collisions. The extension of the NMMA code presented here is the first attempt of analysing the gravitational-wave signal, the kilonovae, and the GRB afterglow simultaneously, which reduces the uncertainty of our constraints. Incorporating all available information, we estimate the radius of a  $1.4M_{\odot}$  neutron star to be  $R = 11.98^{+0.35}_{-0.40}$  km.**

## 1 A New Era in Multi-Messenger Astronomy

The detection of the gravitational-wave (GW) signal GW170817 from the inspiral and merger of two neutron stars (NSs)<sup>1,2</sup> by Advanced LIGO<sup>3</sup> and Advanced Virgo<sup>4</sup>, and of an associated short gamma-ray burst (GRB170817A) by Fermi-GBM<sup>5</sup> and INTEGRAL<sup>6</sup> led to an extensive observational follow-up campaign, enabling different teams to find the resulting kilonova<sup>7</sup> AT2017gfo<sup>8</sup>. The study of the GW and electromagnetic (EM) signals GW170817, AT2017gfo, and GRB170817A has already enabled numerous scientific breakthroughs, for example, constraints on the properties of NSs and the dense matter equation of state (EOS) at supranuclear densities<sup>9–16</sup>, a new and independent measurement of the Hubble constant<sup>15,17–21</sup>, the verified connection between binary NS (BNS) mergers and at least some of the observed short GRBs<sup>22</sup>, and precise limits on the propagation speed of GWs<sup>22</sup>. These scientific achievements were enabled by the multi-messenger nature of GW170817. Despite this enormous progress, results have been obtained by connecting constraints from individual messengers *a posteriori*, i.e., different messengers were analyzed individually and then combined to achieve the final results<sup>13,23–25</sup>. Following this procedure, our previous Nuclear physics - Multi-Messenger Astrophysics (NMMA) framework has been successfully applied to provide new constraints on the EOS of NS matter and on the Hubble constant<sup>15,26</sup>, to investigate the nature of the compact binary merger GW190814<sup>27</sup>, to provide new techniques to search for kilonova transients<sup>28</sup>, to classify observed EM transients such as GRB200826A<sup>29</sup>, and to combine information from multi-messenger observations with data from nuclear-physics experiments such as heavy-ion collisions<sup>16</sup>. Here, we upgrade our framework to allow for simultaneous analysis of kilonova, GRB afterglow, and GW data capitalizing on the multi-messenger nature of compact-binary mergers.

The full potential of our NMMA study becomes clear from Fig. 1 where we show a set of possible EOSs relating the pressure and baryon number density inside NSs. Different constraints can provide valuable information in different density regimes. For example, theoretical calculations of dense nuclear matter in the framework of chiral effective field theory (EFT)<sup>32–36</sup> or data extracted from nuclear-physics experiments, e.g. heavy-ion collisions<sup>37</sup> or the recent PREX-II experiment at Jefferson Laboratory<sup>38</sup>, provide valuable input up to about twice the nuclear saturation density,  $n_{\text{sat}} \sim 0.16 \text{ fm}^{-3}$ . GW signals emitted during the inspiral of a BNS or black-hole–NS (BHNS) systems contain information that probe the EOS at densities realized inside the individual NS components of the system, typically up to about five times  $n_{\text{sat}}$ , but the exact density range probed in such mergers depends noticeably on the mass of the component stars. Furthermore, radio observations of NSs can be used to infer their masses, e.g., by measuring Shapiro delay in a binary system. In particular, radio observations of heavy NSs with masses of about  $\sim 2M_{\odot}$ , such as PSR J0348+0432<sup>39</sup>, PSR J1614-2230<sup>40</sup>, and PSR J0740+6620<sup>41</sup>, provide valuable infor-

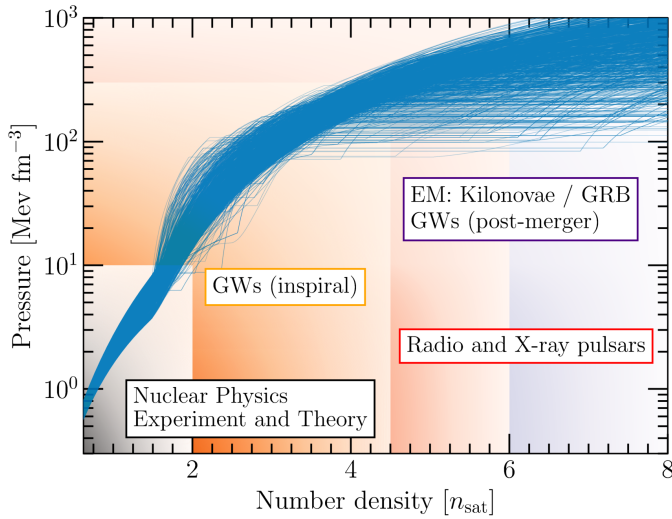


**Figure 1** | Impact of different sources of information on the EOS. We show a set of possible EOSs (blue lines) that are constrained up to  $1.5n_{\text{sat}}$  by Quantum Monte Carlo calculations using chiral EFT interactions<sup>30</sup> and extended to higher densities using a speed of sound model<sup>31</sup>. Different regions of the EOS can then be constrained by using different astrophysical messengers, indicated by rectangles: GWs from inspirals of NS mergers, data from radio and X-ray pulsars, and EM signals associated with NS mergers. Note, that the boundaries are not strict but depend on the EOS and properties of the studied system.

mation at larger densities than those probed by inspiral GW signals. In addition, these observations provide a valuable lower bound on the maximum mass of NSs. Matter at the highest densities in the universe is created in the postmerger phase of a BNS coalescence, i.e., after the collision of the two NSs in the binary. This phase of the binary merger might be observed through future GW detections with more sensitive detectors. Alternatively, this phase can be probed by analyzing EM signals connected to a BNS merger, i.e., the kilonovae, GRBs, and their afterglows. Finally, at asymptotically high densities that are not shown in the figure, the EOSs can be calculated in perturbative QCD<sup>42</sup> and might be used to constrain the NS EOS<sup>43</sup>. The combination of all these various pieces of information provides a unique tool to unravel the properties of matter at supranuclear densities.

## 2 Joint Multi-Messenger Inference

*GW170817-AT2017gfo*: With the NMMA framework, we analyze GW170817 simultaneously with the observed kilonova AT2017gfo. For the GW analysis, we have used the IMRPhenomPv2\_NRTidalv2 waveform model and analyzed the GW data obtained from the Gravitational Wave Open Science Center (GWOSC)<sup>44</sup> in a frequency range of 20Hz to 2048Hz, covering the detected BNS inspiral<sup>45</sup>. For the EM signal, we include the optical, infrared, and ultraviolet data between 0.5 and 10 days days after the merger. The corresponding data is analysed with a Gaussian Process Regression (GPR)-based kilonova model. For our analysis, we are presenting the best fit lightcurve in Fig. 2, with its band representing a 1 magnitude uncertainty for the individual light curves. This 1 magnitude uncertainty is introduced to account for systematic modelling uncertainties<sup>46</sup>.

Fig. 3 summarizes our main findings and shows joint posteriors for the mass of the dynamical ejecta  $m_{\text{dyn}}^{\text{ej}}$ , the mass of the disk wind ejecta  $m_{\text{wind}}^{\text{ej}}$ , the chirp mass  $\mathcal{M}_c$ , the mass ratio  $q$ , the mass-weighted tidal deformability  $\tilde{\Lambda}$ , and the radius of a 1.4 solar mass neutron star  $R_{1.4}$ . In contrast to previous findings using simpler kilonova modelling (see Ref. 47 and references therein), we can fit AT2017gfo with masses

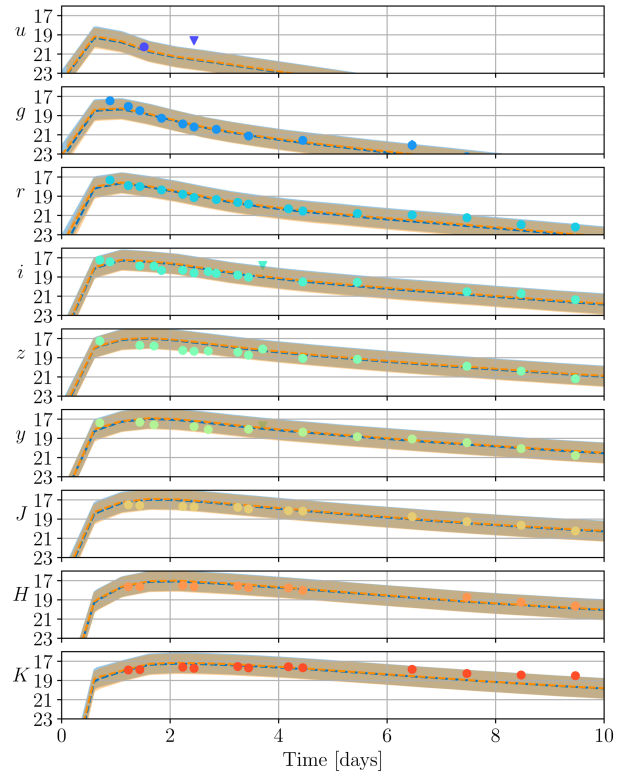


**Figure 2** | Best-fit light curve analysis for AT2017gfo data restricted to lie within 0.5 to 10 days after the BNS merger when analysing GW170817&AT2017gfo (orange) or GW170817&AT2017gfo&GRB170817A (blue) simultaneously. We note that both bands overlap almost completely, i.e., for AT2017gfo the accuracy of the kilonova light curve description does not depend noticeably on the inclusion of a GRB afterglow component.

for the dynamical ( $\sim 0.006 M_{\odot}$ ) and disk-wind ( $\sim 0.07 M_{\odot}$ ) ejecta components that are within the range of values predicted by numerical-relativity simulations<sup>48</sup>. While the parameters extracted are consistent with our previous findings<sup>15</sup>, we observe a clear improvement on the parameter error bounds. This reduction of the credible error bound is even larger than through the inclusion of the kilonova modelling<sup>15,16</sup>. For instance, the constraints on  $R_{1.4} = 11.86_{-0.53}^{+0.41}$ , a typical choice to quantify EOS constraints, is significantly improved compared to our sequential result,  $R_{1.4} = 11.75_{-0.81}^{+0.86}$  km<sup>15</sup>. The half-width of  $R_{1.4}$ 's 90% credible interval decreases from about  $\sim 800$ m<sup>15</sup> to  $\sim 400$ m if GW and EM data are analysed simultaneously instead of sequentially.

*GW170817-AT2017gfo-GRB170817A*: In addition to the combined analysis of GW170817 and AT2017gfo, we can also incorporate information obtained from the GRB afterglow of GW170817A. The GRB afterglow light-curve data are analyzed with the synthetic Gaussian jet-model light curve described before<sup>49,50</sup>. Fig. 2 shows the corresponding best-fit light curve for the kilonova with a 1 magnitude uncertainty band as before. Moreover, we are also presenting the best-fit GRB afterglow light curve and the employed uncertainty band in Fig. 4. We find that both the kilonova AT2017gfo and the GRB afterglow GRB170817A are well described in our analysis.

Fig. 3 again summarizes our findings for the joint posteriors of the mass of the dynamical ejecta, the mass of the disk wind ejecta, the on-axis isotropic equivalent energy, the chirp mass, the mass ratio, the mass-weighted tidal deformability, and the radius of a 1.4 solar mass neutron star for this analysis, which is consistent with GW170817&AT2017gfo only. Compared to the analysis of GW170817&AT2017gfo only, the improvement on the parameter un-

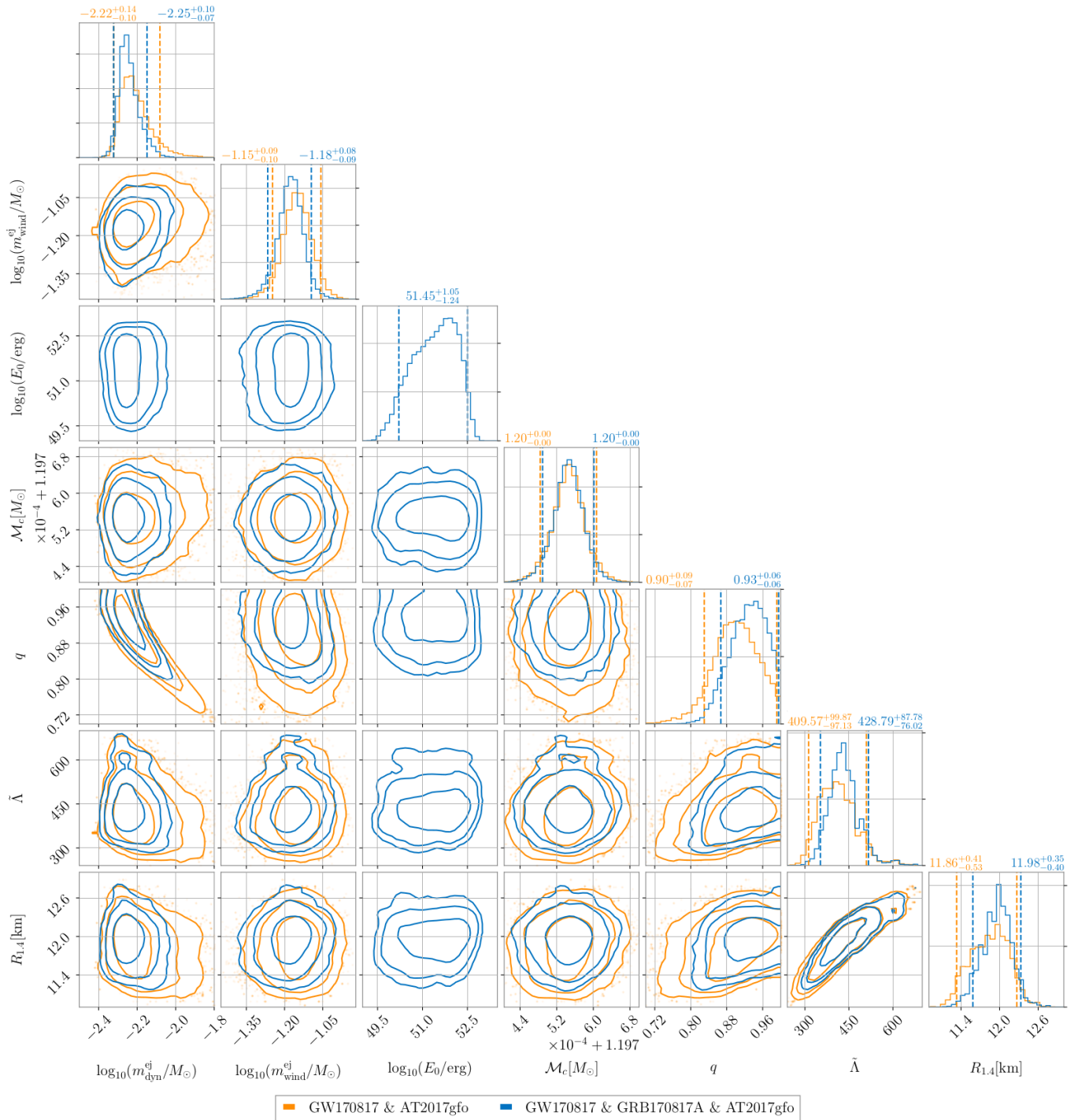


**Figure 3** | Corner plot for the mass of the dynamic ejecta  $m_{\text{dyn}}^{\text{ej}}$ , the mass of the disk wind ejecta  $m_{\text{wind}}^{\text{ej}}$ ,  $\log_{10}$  of the GRB jet on-axis isotropic energy  $\log_{10} E_0$ , the source-frame chirp mass  $\mathcal{M}_c$ , the mass ratio  $q$ , the mass-weighted tidal deformability  $\tilde{\Lambda}$ , and the radius of a 1.4 solar mass neutron star  $R_{1.4}$  at 68%, 95% and 99% confidence. For the 1D posterior probability distributions, we mark the median (solid lines) and the 90% confidence interval (dashed lines) and report these above each panel. We show results that are based on the simultaneous analysis of GW170817&AT2017gfo (orange) and of GW170817&AT2017gfo&GRB170817A (blue).

certainties is only minimal when information from GRB170817A is added. We suspect that this is caused by the fact that the ratio  $\xi$  between the jet energy  $E_0$  and the disk mass  $m_{\text{disk}}$  is taken as a free parameter. Hence, no significant constraint is imposed on the EOS.

### 3 Conclusions

We have developed a new publicly available NMMA framework for the interpretation and analysis of BNS and BHNS systems. This framework allows for the simultaneous analysis of GW and EM signals including kilonovae, supernovae, and GRB afterglows. In addition, our framework allows us to incorporate constraints from nuclear-physics calculations, e.g., by sampling over EOS sets constrained by

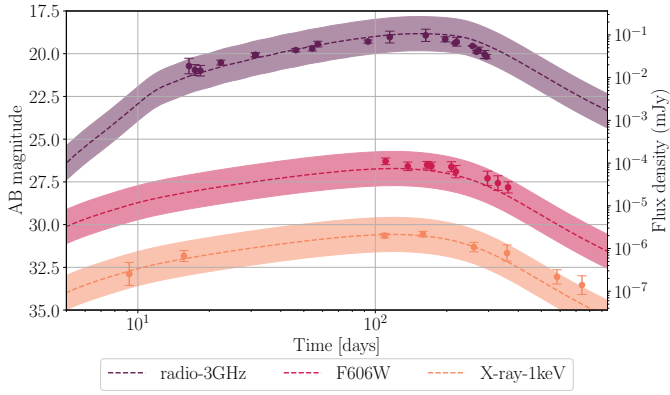


**Figure 4** | Best-fit lightcurve analysis for the analysis of GRB170817A when simultaneously analysing GW170817, AT2017gfo, GRB170817A.

Reference	$R_{1.4M_{\odot}}$ [km]
Dietrich et al. <sup>15</sup>	$11.75^{+0.86}_{-0.81}$ (90%)
Essick et al. <sup>51</sup>	$12.54^{+0.71}_{-0.63}$ (90%)
Breschi et al. <sup>23</sup>	$11.99^{+0.82}_{-0.85}$ (90%)
Nicholl et al. <sup>24</sup>	$11.06^{+1.01}_{-0.98}$ (90%)
Raaijmakers et al. <sup>25</sup>	$12.18^{+0.56}_{-0.79}$ (95%)
Miller et al. <sup>52</sup>	$12.45^{+0.65}_{-0.65}$ (68%)
Huth et al. <sup>16</sup>	$12.01^{+0.78}_{-0.77}$ (90%)
this work [NMMA] <sup>53</sup>	$11.98^{+0.35}_{-0.40}$ (90%)

**Table 1** | Comparison of radius measurements of a  $1.4M_{\odot}$  neutron star for a selection of multi-messenger studies. We denote the corresponding credible interval in parenthesis.

chiral EFT, and to include radio as well as X-ray measurements of isolated NSs. By employing our new framework to a combined analysis of GW170817, AT2017gfo, and GRB170817A, we find that the radius of a typical  $1.4$  solar mass NS lies within  $11.98^{+0.35}_{-0.40}$  km; cf. Tab. 1 for a selection of studies from the literature that (up to our knowledge) used a sequential approach to combine multi-messenger observations. Based on our findings, our analysis is a significant improvement over previous works in which all messengers were analysed sequentially. With the increasing number of multi-messenger detections of BNS and BHNS merger, we expect to use our framework to further increase our knowledge about the interior of NSs.

## 4 Methods

**Equation of State construction.** The EOS describes the relation between energy density  $\varepsilon$ , pressure  $p$ , and temperature  $T$  of dense matter and additionally depends on the composition of the system. For NSs, thermal energies are much smaller than typical Fermi energies of the particles, and therefore, temperature effects can be neglected for isolated NSs or NSs in the inspiral phase of a merger. In these cases, the EOS simply relates  $\varepsilon$  and  $p$ .

The most general constraints on the EOS can be inferred from the slope of the EOS, the speed of sound, defined as

$$c_s = c\sqrt{\partial p/\partial \varepsilon}, \quad (1)$$

where  $c$  is the speed of light. Due to the laws of special relativity, the speed of sound has to be smaller than the speed of light,  $c_s \leq c$ . Furthermore, the speed of sound in a NS has to be larger than zero,  $c_s \geq 0$ , as NSs would otherwise be unstable. These constraints alone, however, allow for an extremely large EOS space.

At nuclear densities, additional information on the EOS can be inferred from laboratory experiments and theoretical nuclear-physics

calculations. For example, this information was used to constrain the properties of stellar matter in the NS crust <sup>54</sup>, i.e., the outermost layer of NSs at densities below  $\sim 0.5n_{\text{sat}}$ . Above  $\sim 0.5n_{\text{sat}}$ , NS matter consists of a fluid of neutrons with a small admixture of protons. In this regime, the EOS can be constrained by microscopic calculations of dense nuclear matter. These calculations typically provide the energy per particle,  $E/A(n, x)$ , which is a function of density  $n$  and proton fraction  $x = n_p/n$  with  $n_p$  being the proton density. From this, the EOS follows from

$$\varepsilon(n, x) = n \frac{E}{A}(n, x), \quad \text{and} \quad p(n, x) = n^2 \frac{\partial E/A(n, x)}{\partial n}. \quad (2)$$

The proton fraction  $x(n)$  is then determined from the beta equilibrium condition,  $\mu_n = \mu_p + \mu_e$ , where  $\mu_i$  is the chemical potential of particle species  $i$ , and  $n$ ,  $p$ , and  $e$  refer to neutrons, protons, and electrons, respectively.

To calculate the energy per particle microscopically, one needs to solve the nuclear many-body problem, commonly described by the Schrödinger equation. This requires knowledge of the nuclear Hamiltonian describing the many-body system. Fundamentally, nuclear many-body systems are described by Quantum Chromodynamics (QCD), the fundamental theory of strong nuclear interactions. QCD describes the system in terms of the fundamental degrees of freedom (d.o.f.), quarks and gluons. Unfortunately, this approach is currently not feasible <sup>55</sup>. At densities of the order of  $n_{\text{sat}}$ , however, the effective d.o.f. are nucleons, neutrons and protons, that can be treated as point-like nonrelativistic particles. Then, the nuclear Hamiltonian can be written generically as

$$H = T + \sum_{i<j} V_{ij}^{\text{NN}} + \sum_{i<j<k} V_{ijk}^{\text{3N}} + \dots, \quad (3)$$

where  $T$  denotes the kinetic energy of the nucleons,  $V_{ij}^{\text{NN}}$  describes two-nucleon (NN) interactions between nucleons  $i$  and  $j$ , and  $V_{ijk}^{\text{3N}}$  describes three-nucleon (3N) interactions between nucleons  $i$ ,  $j$ , and  $k$ . In principle, interactions involving four or more nucleons can be included, but initial studies have found these to be small compared to present uncertainties <sup>56</sup>.

The derivation of the nuclear Hamiltonian (3) from QCD is not feasible due to its nonperturbative nature. In this work, we therefore use a common approach and choose nucleons as effective d.o.f. The interactions among nucleons can then be derived in the framework of Chiral Effective Field Theory (EFT) <sup>57,58</sup>. Chiral EFT starts out with the most general Lagrangian consistent with all the symmetries of QCD in terms of nucleonic degrees of freedom. It explicitly includes meson-exchange interactions for the lightest mesons, i.e., the pions. This approach yields an infinite number of pion-exchange and nucleon-contact interactions which needs to be organized in terms of a hierarchical expansion in powers of a soft (low-energy) scale over a hard (high-energy) scale. In chiral EFT, the soft scale  $q$  is given by the nucleons' external momenta or the pion mass. The hard scale, also called the breakdown scale  $\Lambda_b$ , is of the order of  $500 - 600$  MeV <sup>59</sup> and interaction contributions involving heavier d.o.f., such as the  $\rho$  meson, are integrated out. The chiral Lagrangian is then expanded in powers of  $q/\Lambda_b$  according to a power-counting scheme. Most current chiral EFT interactions are derived in Weinberg power counting <sup>57,58,60-62</sup>. One can then derive the nuclear Hamiltonian from this chiral Lagrangian in a consistent order-by-order framework that allows for an estimate of the theoretical uncertainties <sup>59,63,64</sup> and that can be systematically improved by increasing the order of the calculation. Chiral EFT Hamiltonian naturally include NN, 3N, and higher many-body forces, see Eq. (3), and chiral EFT predicts a natural hierarchy of these contributions. For example, 3N interactions start to contribute at third order ( $N^2\text{LO}$ ) in the expansion. Typical state-of-the-art calculations truncate the chiral expansion at  $N^2\text{LO}$  <sup>32,35,65</sup> or fourth order ( $N^3\text{LO}$ ) <sup>34,66</sup>.

With the nuclear Hamiltonian at hand, one then needs to solve the many-body Schrödinger equation which requires advanced numerical methods. Examples of such many-body techniques include many-body perturbation theory (MBPT)<sup>33,34,66</sup>, the self-consistent Green’s function (SCGF) method<sup>67</sup>, or the coupled-cluster (CC) method<sup>65,68</sup>. Here, we employ Quantum Monte Carlo (QMC) methods<sup>69</sup>, which provide nonperturbative solutions of the Schrödinger equation. QMC methods are stochastic techniques which treat the Schrödinger equation as a diffusion equation in imaginary time. In the QMC framework, one begins by choosing a trial wavefunction of the many-body system, which for nuclear matter can be described as a Slater determinant of non-interacting fermions multiplied with NN and 3N correlation functions. This trial wavefunction is evolved to large imaginary times, projecting out high-energy excitations, and converging to the true ground state of the system as long as the trial wavefunction has a non-zero overlap with it. Among QMC methods, two well-established algorithms are Green’s function Monte Carlo (GFMC), used to describe light atomic nuclei with great precision<sup>69</sup>, and Auxiliary Field Diffusion Monte Carlo (AFDMC)<sup>70</sup>, suitable to study larger systems such as nuclear matter. Here, we employ AFDMC calculations of neutron matter but our NMMA framework is sufficiently flexible to employ any low density calculation for neutron-star matter.

At nuclear densities, chiral EFT together with a suitable many-body framework provides for a reliable description of nuclear matter with systematic uncertainty estimates. With increasing density, however, the associated theoretical uncertainty grows fast due to the correspondingly larger nucleon momenta approaching the breakdown scale. The density up to which chiral EFT remains valid is not exactly known but estimates place it around  $2n_{\text{sat}}$ <sup>30,59</sup>. Hence, chiral EFT calculations constrain the EOS only up to these densities but to explore the large EOS space beyond the breakdown of chiral EFT, one requires a physics-agnostic extension scheme. Here, physics-agnostic implies that no model assumptions, e.g., about the existence of certain d.o.f. at high densities, are made. Instead, the EOS is only bounded by conditions of causality,  $c_S \leq c$ , and mechanical stability,  $c_S \geq 0$ , mentioned before. There exist several such extension schemes in literature: parametric ones, like the polytropic expansion<sup>71–73</sup> or expansions in the speed of sound<sup>74,75</sup>, and nonparametric approaches<sup>76</sup>. To extend the AFDMC calculations employed here, we employ a parametric speed-of-sound extension scheme. Working in the  $c_S$  versus  $n$  plane, the speed of sound  $c_S(n)$  is determined with theoretical uncertainty estimates by chiral EFT up to a reference density below the expected breakdown density. From this uncertainty band, we sample a speed-of-sound curve up to the reference density. Beyond this density, we create a typically non-uniform grid in density up to a large density  $\approx 12n_{\text{sat}}$ , well beyond the regime realized in NSs. For each grid point, we sample random values for  $c_s^2(n_i)$  between 0 and  $c^2$  (we set  $c = 1$  in the following). We then connect the chiral EFT draw for the speed of sound with all points  $c_{s,i}^2(n_i)$  using linear segments. The resulting density-dependent speed of sound can be integrated to give the EOS, i.e., the pressure, baryon density, and energy density. In the interval  $n_i \leq n \leq n_{i+1}$ ,

$$p(n) = p(n_i) + \int_{n_i}^n c_s^2(n') \mu(n') dn', \quad (4)$$

$$\epsilon(n) = \epsilon(n_i) + \int_{n_i}^n \mu(n') dn', \quad (5)$$

where  $\mu(n)$  is the chemical potential that can be obtained from the speed of sound using the relation

$$\mu(n) = \mu_i \exp \left[ \int_{\log n_i}^{\log n} c_s^2(\log n') d \log n' \right]. \quad (6)$$

For each reconstructed EOS, constrained by Chiral EFT at low densities and extrapolated via the  $c_S$  extension to larger densities, the global properties of NSs can be calculated by solving the Tolman–Oppenheimer–Volkoff (TOV) equations. This way, we determine the NS radii ( $R$ ) and dimensionless tidal deformabilities ( $\Lambda$ ) as functions of their masses ( $M$ ). We repeat this approach for a large number of samples to construct EOS priors for further analyses of NS data.

This approach is flexible and additional information on high-density phases of QCD can be included straightforwardly. For example, pQCD calculations at asymptotically high densities<sup>42</sup>, of the order of  $40 - 50n_{\text{sat}}$ , might be used to constrain the general EOS extension schemes even further<sup>43,73</sup>. However, the exact impact of these constraints at densities well beyond the regime realized in NSs needs to be studied in more detail. While our NMMA framework currently does not have this capability, we are planning to add this in the near future. Similarly, instead of using general extension models, one can employ specific high-density models accounting for quark and gluon d.o.f. One such model is the quarkyonic-matter model<sup>77–80</sup>, which describes the observed behavior of the speed of sound in NSs<sup>30</sup>: a rise of the speed of sound at low densities to values above the conformal limit of  $c/\sqrt{3}$ , followed by a decrease to values below the conformal limit at higher densities. In future work, we will address quarkyonic matter and other models in our NMMA framework.

The construction of the EOS, as detailed above, is implemented in the NMMA code under the class `EOS_with_CSE`. This class allows for (a) an exploration of theoretical uncertainties in the low-density EOS and (b) constructs the high-density EOS using a  $c_S$  extrapolation. (a) Low-density uncertainties are implemented by requiring two tabulated EOS files for the lower and upper bound of the uncertainty band as inputs, containing the pressure, energy density and number density up to the chosen breakdown density of the model. By default, the results of a QMC calculation using local chiral EFT interactions at  $N^2\text{LO}$ <sup>30</sup> with theoretical uncertainties are provided. Upon initiation of the class, a sample is drawn from the low-density uncertainty band using a 1-parameter sampling technique. In this approach, a uniform random number  $\omega$  is sampled uniformly between 0 and 1, and the interpolated EOS is given as

$$p(n) = p_{\text{soft}}(n) + \omega(p_{\text{stiff}}(n) - p_{\text{soft}}(n)), \quad (7)$$

$$\epsilon(n) = \epsilon_{\text{soft}}(n) + \omega(\epsilon_{\text{stiff}}(n) - \epsilon_{\text{soft}}(n)), \quad (8)$$

where the subscripts “soft” and “stiff” refer to the lower and upper bounds of the EFT uncertainty band, respectively. This sampling technique assumes that pressure and energy density are correlated but we have found that releasing this assumption and using a four-parameter form suggested by Gandolfi et al.<sup>81</sup> does not change our results appreciably. In future, we will explore additional schemes, e.g., using Gaussian processes<sup>51</sup>.

(b) The EOS given by Eqs. (7) and (8) is used up to a breakdown density determined by the user. By default, this density is set to  $2n_{\text{sat}}$ . Beyond this density, the class constructs the EOS using a  $c_S$  extension. The maximum density up to which the EOS is extrapolated and the number of linear line segments can be adjusted by the user, with the default values being  $12n_{\text{sat}}$  for the former and 5 line segments for the latter. The code then solves Eqs. (4), (5) and (6) to give the extrapolated EOS. The pressure, energy density, and number density describing the full EOS are accessible as attributes of the `EOS_with_CSE` class.

Finally, the method `construct_family` solves the stellar structure equations (TOV equations and equations for the quadrupole perturbation of spherical models), and returns a sequence of NSs with their masses, radii and dimensionless tidal deformabilities as arrays.

**Prior weighting to incorporate radio and X-ray observations of single neutron stars.** To incorporate mass measurements of heavy

pulsars and mass-radius measurements of isolated pulsars, the associated likelihood is calculated and taken as the prior probability for an EOS for further analysis. For instance, the radio observations on PSR J0348+4042<sup>39</sup>, and PSR J1614-2230<sup>40</sup> provide a lower bound on the maximum mass of a NS.

The likelihood for a mass-only measurement is given by

$$\mathcal{L}_{\text{PSR-mass}}(\vec{E}) = \int_0^{M_{\text{TOV}}} dM \mathcal{P}(M|\text{PSR}), \quad (9)$$

where  $\mathcal{P}(M|\text{PSR})$  is the posterior distribution of the pulsar's mass and  $M_{\text{TOV}}$  is the maximum mass supported by the EOS with parameters  $\vec{E}$ . The posterior distributions of pulsar masses are typically well approximated by Gaussians<sup>15</sup>.

Recent X-ray observations of millisecond pulsars by NASA's Neutron Star Interior Composition Explorer (NICER) mission have been used to simultaneously determine the mass and radius of these NSs<sup>52,82-85</sup>. The corresponding likelihood is given by

$$\begin{aligned} \mathcal{L}_{\text{NICER}}(\vec{E}) &= \int dM \int dR \mathcal{P}_{\text{NICER}}(M, R) \frac{\pi(M, R|\vec{E})}{\pi(M, R|I)} \\ &\propto \int dM \int dR \mathcal{P}_{\text{NICER}}(M, R) \delta(R - R(M; \vec{E})) \\ &\propto \int dM \mathcal{P}_{\text{NICER}}(M, R = R(M; \vec{E})), \end{aligned} \quad (10)$$

where  $\mathcal{P}_{\text{NICER}}(M, R)$  is the joint-posterior distribution of mass and radius as measured by NICER and we use the fact that (i) the radius is a function of mass for a given EOS, and (ii) that without further EOS information, e.g., through chiral EFT, the prior for the radius given mass is taken to be uniform.

### Gravitational-wave inference.

*GW models:* A complex frequency-domain GW signal is given by

$$h(f) = A(f)e^{-i\psi(f)}, \quad (11)$$

with the amplitude  $A(f)$  and the GW phase  $\psi(f)$ . Because of the NS's finite size and internal structure, BNS and BHNS waveform models have to incorporate tidal contributions for an accurate interpretation of the binary coalescence. Such tidal contributions account for the deformation of the stars in their companions' external gravitational field<sup>86,87</sup> and, once measured, allow to place constraints on the EOS governing the NS interior<sup>1,88-90</sup>. They are attractive because they convert energy from the orbital motion to a deformation of the stars, and lead to an accelerated inspiral. In the case of non-spinning compact objects, the leading-order tidal contribution depends on the tidal deformability

$$\tilde{\Lambda} = \frac{16(m_1 + 12m_2)m_1^4\Lambda_1 + (m_2 + 12m_1)m_2^4\Lambda_2}{(m_1 + m_2)^5} \quad (12)$$

with the individual tidal deformabilities  $\Lambda_{1,2} = \frac{2}{3}k_2^{1,2}/C_{1,2}^5$  and the individual masses  $m_{1,2}$ . Here,  $k_2^{1,2}$  are the Love numbers describing the static quadrupole deformation of one body inside the gravitoelectric field of the companion and  $C_{1,2}$  are the individual compactnesses  $C_{1,2} = m_{1,2}/R_{1,2}$  in isolation.

To date, there are three different types of BNS or BHNS models for the inspiral GW signal that are commonly used: Post-Newtonian (PN) models<sup>91-94</sup>, effective-one-body (EOB) models<sup>95-103</sup>, and phenomenological approximants<sup>104-108</sup>. In the NMMA framework, we make use of the LALSuite<sup>109</sup> software package, in particular LALSimulation, so that the BNS and BHNS models used by the LIGO-Virgo-Kagra Collaborations can be easily employed. This includes:

- PN models such as TaylorT2, TaylorT4, or TaylorF2 where a PN descriptions for the point-particle BBH baseline as well as the tidal description is employed,
- the most commonly used tidal EOB models SEOBNRv4T<sup>98,103,110</sup>, its frequency-domain surrogate model<sup>111</sup>, as well as the TEOBResumS model<sup>99,112</sup> including its post-adiabatic accelerated version<sup>113</sup> which enables it being used during parameter estimation,
- and phenomenological models such as IMRPhenomD\_NRTidal, SEOBNRv4\_ROM\_NRTidal, IMRPhenomPv2\_NRTidal, IMRPhenomD\_NRTidalv2, SEOBNRv4\_ROM\_NRTidalv2, IMRPhenomPv2\_NRTidalv2<sup>105-107</sup>, PhenomNSBH, and SEOBNRv4\_ROM\_NRTidalv2\_NSBH<sup>108,114</sup>.

*GW analysis:* By assuming stationary Gaussian noise, the GW likelihood  $\mathcal{L}_{\text{GW}}(\vec{\theta})$  that the data  $d$  is a sum of noise and a GW signal  $h$  with parameters  $\vec{\theta}$  is given by<sup>115</sup>

$$\mathcal{L}_{\text{GW}} \propto \exp\left(-\frac{1}{2}\langle d - h(\vec{\theta}) | d - h(\vec{\theta}) \rangle\right), \quad (13)$$

where the inner product  $\langle a|b \rangle$  is defined as

$$\langle a|b \rangle = 4\Re \int_{f_{\text{low}}}^{f_{\text{high}}} \frac{\tilde{a}(f)\tilde{b}^*(f)}{S_n(f)} df. \quad (14)$$

Here,  $\tilde{a}(f)$  is the Fourier transform of  $a(t)$ , \* denotes complex conjugation, and  $S_n(f)$  is the one-sided power spectral density of the noise. The choice of  $f_{\text{low}}$  and  $f_{\text{high}}$  depends on the type of binary that we are interested in. In our study, we will set  $f_{\text{low}}$  and  $f_{\text{high}}$  to 20 Hz and 2048 Hz, respectively. This is sufficient for capturing the inspiral up to the moment of merger for a typical BNS system in the advanced GW detector era.

### Electromagnetic Signals: Kilonovae and Supernovae.

*Kilonova models:* Kilonova models are extracted using the 3D Monte Carlo radiative transfer code POSSIS<sup>116</sup>. The code can handle arbitrary geometries for the ejected material and produces spectra, light curves and polarization as a function of the observer viewing angle. Given an input model with defined densities  $\rho$  and compositions (i.e., electron fraction  $Y_e$ ), the code generates Monte Carlo photon packets with initial location and energy sampled from the energy distribution from radioactive decay of r-process nuclei within the model. The latter depends on the mass/density distribution of the model and the assumed nuclear heating rates and thermalization efficiencies. The frequency of each Monte Carlo photon packet is sampled according to the temperature  $T$  in the ejecta, which is calculated at each time-step<sup>117,118</sup>. Photon packets are then followed as they diffuse out of the ejected material and interact with matter via either electron scattering or bound-bound line transitions. Time- and wavelength-dependent opacities  $\kappa_\lambda(\rho, T, Y_e, t)$  from Tanaka et al.<sup>119</sup> are implemented in the code and depend on the local properties of the ejecta ( $\rho$ ,  $T$ , and  $Y_e$ ). Spectral time series are extracted using the technique described by Bulla et al.<sup>120</sup> and used to construct broad-band light curves in any desired filter.

*Supernova models:* Templates available within the SNCosmo library<sup>121</sup> are used to model supernova spectra. Currently, the salt2 model for Type Ia supernovae and the nugent-hyper model for hypernovae associated with long GRBs are implemented in the framework and have been used in the past<sup>29</sup>. However, the framework is flexible enough such that additional templates for different types of supernovae can be added with minimal effort.

*Kilonova/Supernova Inference:* Our EM inference of kilonovae and GRB afterglows is based on the AB magnitude for a specific filter  $j$ ,  $m_i^j(t_i)$ . We assume these measurements to be given as a time series at times  $t_i$  with a corresponding statistical error  $\sigma_i^j \equiv \sigma^j(t_i)$ . The likelihood function  $\mathcal{L}_{\text{EM}}(\vec{\theta})$  then reads<sup>122</sup>:

$$\mathcal{L}_{\text{EM}} \propto \exp\left(-\frac{1}{2} \sum_{ij} \left(\frac{m_i^j - m_i^{j,\text{est}}(\vec{\theta})}{\sigma_i^j}\right)^2\right), \quad (15)$$

where  $m_i^{j,\text{est}}(\vec{\theta})$  is the estimated AB magnitude for the parameters  $\vec{\theta}$ .

For kilonovae, we use the same model presented in Dietrich et al.<sup>15</sup>. The model is controlled by four parameters, namely, the dynamical ejecta mass  $m_{\text{dyn}}^{\text{ej}}$ , the disk wind ejecta mass  $m_{\text{wind}}^{\text{ej}}$ , the half-opening angle of the lanthanide-rich component  $\Phi$ , and the viewing angle  $\theta_{\text{obs}}$ . Both the dynamical ejecta and the disk wind ejecta are described in Sec. 4.

**Electromagnetic Signals: GRB Afterglows.** In our framework, the computation of the GRB afterglow light curves is until now based on the publicly available semi-analytic code `afterglowpy`<sup>49,50</sup>. The inclusion of other afterglow models is currently ongoing.

The GRB afterglow emission is produced by relativistic electrons gyrating around the magnetic field lines. These electrons are accelerated by the Fermi first-order acceleration (diffusive shock acceleration) and the magnetic field is assumed to be of turbulent nature, amplified by processes acting in collision-less shocks. The complex physics of electron acceleration at shocks is approximated by the equipartition parameters,  $\epsilon_e$  and  $\epsilon_B$ , denoting the fraction of the shock energy that goes into the relativistic electrons and magnetic field, respectively, and  $p$ , and the slope of the electron energy distribution  $dn/d\gamma \propto \gamma^{-p}$ , with  $n$  being the electron number density and  $\gamma$  being the electron Lorentz factor. The flux density of the curvature radiation is

$$F_\nu = \frac{1}{4\pi d_L^2} \int d\theta d\phi R^2 \sin(\theta) \frac{\epsilon_\nu}{\alpha_\nu} (1 - e^{-\tau}), \quad (16)$$

where  $\tau$  is the optical depth and  $\epsilon_\nu$  and  $\alpha_\nu$  are the impassivity coefficient and absorption coefficient, respectively. For a fixed power-law distribution of electrons these can be approximated analytically<sup>123</sup>. The synchrotron self-absorption is neglected in this work.

In order to capture the possible dependence of the GRB properties on the polar angle, the jet is discretized into a set of lateral axisymmetric (conical) layers, each of which is characterized by its initial velocity, mass, and angle. Several prescriptions for the initial angular distribution of the jet energy are available in the code. As default, we use the Gaussian jet model with  $E \propto E_0 \exp(-\frac{1}{2}(\frac{\theta}{\theta_c})^2)$ , where  $\theta_c$  characterizes the width of the Gaussian. We assume the GRB jet to be powered by the accretion of mass from the disk onto the remnant black hole<sup>124–127</sup>. Consequently, the jet energy is proportional to the leftover disk mass,

$$E_0 = \epsilon \times (1 - \xi) \times m_{\text{disk}}, \quad (17)$$

where  $\xi$  is the fraction of disk mass ejected as wind and  $\epsilon$  is the fraction of residual disk mass converted into jet energy.

The dynamical evolution of these layers is computed semi-analytically using the “thin-shell approximation” casting energy-conservation equations and shock-jump conditions into a set evolution equations for the blast wave velocity and radius. Within blast waves, the pressure gradient perpendicular to the normal leads to lateral expansion<sup>128,129</sup>. In other words, the transverse pressure gradient ads the velocity along the tangent to the blast wave surface, forcing the latter to expand. The lateral expansion is important for late-time afterglow and is included in the code.

Finally, the flux density,  $F_\nu$ , is obtained by equal arrival time surface integration, Eq. (16), taking into account relativistic effects,

i.e., that the observed  $F_\nu$  is composed of contributions from different blast waves that has emitted at different comoving time and at different frequencies.

**Connecting Electromagnetic Signals to Source properties.** To connect the observed GRB, kilonova, and GRB afterglow properties to the binary properties, we rely on phenomenological relations, i.e., fits based on numerical-relativity simulations. For our work, we use the fits presented in Kruger et al.<sup>130</sup> and Dietrich et al.<sup>15</sup> but emphasize that a variety of other fitting formulas exist in the literature<sup>13,48,131–133</sup>.

In NMMA, the dynamical ejecta mass  $m_{\text{dyn}}^{\text{ej}}$  is connected to the binary properties through the phenomenological relation<sup>130</sup>

$$\frac{m_{\text{dyn,fit}}^{\text{ej}}}{10^{-3}M_\odot} = \left(\frac{a}{C_1} + b\left(\frac{m_2}{m_1}\right)^n + cC_1\right) + (1 \leftrightarrow 2), \quad (18)$$

where  $m_i$  and  $C_i$  are the masses and the compactness of the two components of the binary with best-fit coefficients  $a = -9.3335$ ,  $b = 114.17$ ,  $c = -337.56$ , and  $n = 1.5465$ . This relation enables an accurate estimation of the ejecta mass with an error well-approximated by a zero-mean Gaussian with a standard deviation  $0.004M_\odot$ <sup>130</sup>. Therefore, the dynamical ejecta mass can be approximated as

$$m_{\text{dyn}}^{\text{ej}} = m_{\text{dyn,fit}}^{\text{ej}} + \alpha, \quad (19)$$

where  $\alpha \sim \mathcal{N}(\mu = 0, \sigma = 0.004M_\odot)$ .

To determine the disk mass  $m_{\text{disk}}$ , we follow the description of Dietrich et al.<sup>15</sup>,

$$\log_{10}\left(\frac{m_{\text{disk}}}{M_\odot}\right) = \quad (20)$$

$$\max\left(-3, a\left(1 + b \tanh\left(\frac{c - (m_1 + m_2)M_{\text{threshold}}^{-1}}{d}\right)\right)\right), \quad (21)$$

with  $a$  and  $b$  given by

$$a = a_o + \delta a \cdot \Delta, \quad b = b_o + \delta b \cdot \Delta, \quad (22)$$

where  $a_o, b_o, \delta a, \delta b, c$ , and  $d$  are free parameters. The parameter  $\Delta$  is given by

$$\Delta = \frac{1}{2} \tanh(\beta(q - q_{\text{trans}})), \quad (23)$$

where  $q \equiv m_2/m_1 \leq 1$  is the mass ratio and  $\beta$  and  $q_{\text{trans}}$  are free parameters. The best-fit model parameters are  $a_o = -1.581$ ,  $\delta a = -2.439$ ,  $b_o = -0.538$ ,  $\delta b = -0.406$ ,  $c = 0.953$ ,  $d = 0.0417$ ,  $\beta = 3.910$ ,  $q_{\text{trans}} = 0.900$ . The threshold mass  $M_{\text{threshold}}$  for a given EOS is estimated as<sup>134</sup>

$$M_{\text{threshold}} = \left(2.38 - 3.606 \frac{M_{\text{TOV}}}{R_{1.6}}\right) M_{\text{TOV}}, \quad (24)$$

where  $M_{\text{TOV}}$  and  $R_{1.6}$  are the maximum mass of a non-spinning NS and the radius of a  $1.6M_\odot$  NS. We note that we assume that the disk-wind ejecta component is proportional to the disk mass, i.e.,  $m_{\text{wind}}^{\text{ej}} = \xi \times m_{\text{disk}}$ .

**Bayesian statistics.** Based on Bayes’ theorem, the posterior distribution of the parameters  $p(\vec{\theta}|d, \mathcal{H})$  under hypothesis  $\mathcal{H}$  with data  $d$  is given by

$$p(\vec{\theta}|d, \mathcal{H}) = \frac{p(d|\vec{\theta}, \mathcal{H})p(\vec{\theta}|\mathcal{H})}{p(d|\mathcal{H})} \equiv \frac{\mathcal{L}(\vec{\theta})\pi(\vec{\theta})}{\mathcal{Z}(d)}, \quad (25)$$

where  $\mathcal{L}(\vec{\theta})$ ,  $\pi(\vec{\theta})$ , and  $\mathcal{Z}(d)$  are the likelihood, prior, and evidence, respectively. The prior describes our knowledge of the source or model parameters prior to the experiment or observation. The likelihood and evidence quantify how well the hypothesis describes the data for a

given set of parameters and over the whole parameter space, respectively. Throughout our NMMA pipeline, all data analyses use Bayes' theorem but differences appear due to the functional form of the likelihood and its specific dependence on the source parameters. For example, the GW likelihood is evaluated with a cross-correlation between the data and the GW waveform and the EM signal analysis employs a  $\chi^2$  log-likelihood between the predicted light curves with the observed apparent magnitude data, however, from a Bayesian viewpoint their treatment is equivalent only with different likelihood functions.

In addition to the posterior estimation, the evidence  $\mathcal{Z}$  carries additional information on the plausibility of a given hypothesis  $\mathcal{H}$ . The evidence is given by

$$\mathcal{Z}(d|\mathcal{H}) = \int d\vec{\theta} p(d|\vec{\theta}, \mathcal{H}) p(\vec{\theta}|\mathcal{H}) = \int d\vec{\theta} \mathcal{L}(\vec{\theta}) \pi(\vec{\theta}), \quad (26)$$

which is the normalization constant for the posterior distribution. Moreover, we can compare the plausibilities of two hypotheses,  $\mathcal{H}_1$  and  $\mathcal{H}_2$ , by using the odd ratio  $\mathcal{O}_2^1$ , which is given by

$$\mathcal{O}_2^1 = \frac{\mathcal{Z}_1 p(\mathcal{H}_1)}{\mathcal{Z}_2 p(\mathcal{H}_2)} \equiv \mathcal{B}_2^1 \Pi_2^1, \quad (27)$$

where  $\mathcal{B}_2^1$  and  $\Pi_2^1$  are the Bayes factor and prior odds, respectively. If  $\mathcal{O}_2^1 > 1$ ,  $\mathcal{H}_1$  is more plausible than  $\mathcal{H}_2$ , and vice versa.

## 5 Technical Framework

### Computing generic kilonova lightcurves.

*Gaussian Process Regression:* Because we are given vectors of photometry or spectra from radiative transfer simulations, we require methods to interpolate between these grids. If we denote the parameters of the models as  $\vec{\Theta}^j$  and the vectors of data as  $\tau$ , parameterized by the  $i$ -th time index, we can create matrices of simulations as  $\mathcal{T}_{ij} = [\tau_i(\vec{\Theta}^j)]$ . From these matrices, there are a variety of ways to interpolate these vectors, including direct interpolation of the vectors. Here, instead, we interpolate the principal components of each  $\tau_i$ . To compute the principal components, we take the singular value decomposition (SVD) of this matrix

$$\mathcal{T} = V \Sigma U^\top. \quad (28)$$

The SVD computes orthonormal basis vectors in the columns and rows of  $V$  and  $U$ . With this new basis, we can project our original  $\tau_i$  onto the left-singular vector basis

$$s_k(\vec{\Theta}^j) = V_{ki}^\top \tau_i(\vec{\Theta}^j), \quad (29)$$

where  $s_k$  are the weights of the principal components of the input data  $\mathcal{T}_{ij}$ . This method has the benefit of maximizing the variance in each subsequent basis vector, meaning we can truncate this sum to minimize computational resources; in our case, we find that using the first 10 basis vectors is sufficient for a reliable representation of the light curves.

To interpolate the principal component eigenvalues, we use Gaussian process regression (GPR) <sup>135</sup>, which relies on the assumption that the correlation between neighboring values can be represented by a multivariate Gaussian distribution. The covariance between function values is known as a ‘kernel’ function, with many kernel functions commonly used in the literature; in our analysis, we use a rational-quadratic kernel function implemented in `sci-kit learn` <sup>136</sup>:

$$k(\vec{\Theta}^i, \vec{\Theta}^j) = \left( 1 + \frac{d(\vec{\Theta}^i, \vec{\Theta}^j)^2}{2\alpha l^2} \right)^{-\alpha} \quad (30)$$

where  $\alpha = 0.1$  and  $l = 1.0$  for our implementation.

As is common in GPR-based interpolation, we first normalize the components of  $s_k(\vec{\Theta}^j)$  by subtracting the minimum value and dividing by the difference between the maximum and minimum value. After the interpolation, the de-whitened values are projected back into the time domain:

$$\tau_i(\vec{\Theta}^j) = V_{ik} s_k(\vec{\Theta}^j) \quad (31)$$

Finally, the interpolated  $\tau_i(\vec{\Theta}^j)$  is then used for the computation of the likelihood.

*Neural Networks:* Another alternative method for the grid interpolation is a feed-forward neural network (NN) which can predict the kilonova light curves based on the input parameters used by the chosen model <sup>137</sup>. The main advantage of this approach is it to reduce the memory footprint for the light curves computation.

To train the NN, we use about 2000 lightcurves computed with the full radiative transfer code POSSIS <sup>116</sup>. These lightcurves are split into a training data set of 90% and an evaluation dataset that contains 10% of all lightcurves. In the pre-processing stage, all the data was normalized between 0 and 1 via the usual MinMax normalization method, and similar to the GPR method, we used PCA data reduction to reduce the dimensions of the output parameter space to 10 components. In addition, we use simple linear interpolation for the cases in which the requested time interval is larger than the original in-hand data.

To develop our NN, we used Keras API from TENSORFLOW <sup>138</sup>. Our NN comprises an input layer with the same number of neurons as the input parameter space, three dense hidden layers with 64, 128, and 128 neurons each, and an output layer with ten neurons for the bolometric luminosity and the nine observational bands. We use the Adam optimizer with a learning rate of 0.01 and a Rectified linear unit as activation function. Finally, the NN is trained using a batch size of 32, epoch count of 15, and mean squared error (MSE) as loss function. To reconstruct the real light curves, a series of inverse transformations is applied with respect to the PCA and the normalization. Overall a MSE of 0.0022 is achieved.

**EOS Sampling.** For a set of EOSs, such as our sets constrained by chiral EFT, our framework is able to directly sample over EOSs instead of sampling over the masses and tidal deformabilities independently. Since these EOSs relate masses and tidal deformabilities based on nuclear-physics information, the tidal deformabilities can be computed for a given mass and EOS according to

$$p(\Lambda_i | m_i, \text{EOS}) = \delta(\Lambda_i - \Lambda(m_i; \text{EOS})). \quad (32)$$

This feature enables the possibility to include more physical information on the NS sources during parameter estimation *ab initio* and can be used through the installation of additional BILBY and PARALLEL BILBY patches that come along with our NMMA framework. Another advantage of this functionality is that information from multiple simulations can be combined to compute a combined posterior because the EOS is a common parameter for all NSs <sup>139</sup>.

**Combined Sampling.** To extract most information from the GW and the EM data, we perform a full parameter estimation combining both likelihoods. The ‘full’ likelihood  $\mathcal{L}$  is given by

$$\mathcal{L}(\vec{\theta}) = \mathcal{L}_{\text{GW}}(\vec{\theta}_{\text{GW}}) \times \mathcal{L}_{\text{EM}}(\vec{\theta}_{\text{EM}}), \quad (33)$$

where  $\vec{\theta} = \{\vec{\theta}_{\text{GW}}, \vec{\theta}_{\text{EM}}\}$ . Because the light curve models and the GW waveform models depend on different sets of parameters, simply sampling over all of the parameters would not yield a stronger constraint on the parameters of interest. Therefore, it is key to use connections between different parameters at the prior level. In particular, a few parameters describing the EM signals can be determined by the binary



Parameter	Name	Connection with other parameters
$m_i$	Component mass	-
EOS	Equation-of-state of the nuclear matter	-
$\bar{s}_i$	Component spin	-
$\Lambda_i$	Tidal deformability	$\Lambda_i = \Lambda(m_i; \text{EOS})$
$C_i$	Compactness	$C_i = C(m_i; \text{EOS})$
$\alpha$	Dynamic ejecta mass fitting error	-
$m_{\text{dyn}}^{\text{ej}}$	Dynamic ejecta mass	$m_{\text{dyn}}^{\text{ej}} = m_{\text{dyn,fit}}^{\text{ej}}(m_i, C_i) + \alpha$
$M_{\text{threshold}}$	Threshold mass	$M_{\text{threshold}} = M_{\text{threshold}}(\text{EOS})$
$m_{\text{disk}}$	Disk mass	$m_{\text{disk}} = m_{\text{disk}}(m_i, M_{\text{threshold}})$
$\xi$	Fraction of the disk mass to be ejected as wind	-
$m_{\text{wind}}^{\text{ej}}$	Wind ejecta mass	$m_{\text{wind}}^{\text{ej}} = \xi \times m_{\text{disk}}$
$\Phi$	Lanthanide-rich composition opening angle	-
$\epsilon$	Fraction of leftover disk mass to be converted to GRB jet	-
$E_0$	GRB jet on-axis isotropic energy	$E_0 = \epsilon \times (1 - \xi) \times m_{\text{disk}}$
$\theta_c$	Half-width of the jet core	-
$\theta_w$	Truncation angle of the jet	-
$n_0$	Number density of ISM	-
$p$	Electron distribution power-law index	-
$\epsilon_e$	Thermal energy fraction in electrons	-
$\epsilon_B$	Thermal energy fraction in magnetic field	-

**Table 2** | Table summarizing the intrinsic parameters for the multi-messenger observation of a BNS merger.

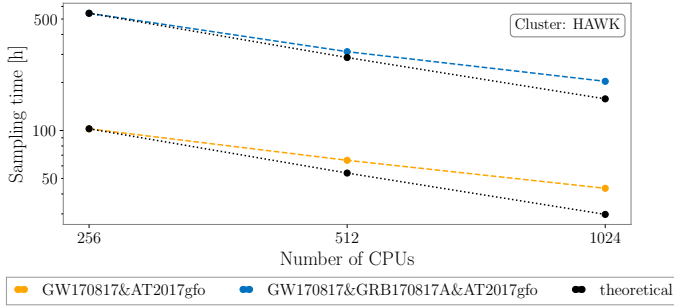


**Figure 5** | Theoretical vs. measured scaling performance for the inference runs of GW170817-AT2017gfo and GW170817-GRB170817A-AT2017gfo on 256, 512, and 1024 cores, respectively. The theoretical scaling is computed for 256 cores using the reference time  $T(N_{\text{core,ref}}) = 102.49$  h for GW170817-AT2017gfo and  $T(N_{\text{core,ref}}) = 543.45$  h for GW170817-GRB170817A-AT2017gfo.

masses and the EOS. For instance, the dynamic ejecta mass  $m_{\text{dyn}}^{\text{ej}}$  and the disk mass  $m_{\text{disk}}$  are connected to the binary properties through the relations discussed in Sec. 4. The details for all the parameters are summarized in Tab. 2.

**Scaling.** Due to the enormous computational burden of simultaneously analysing both the EM and GW signals, we have to ensure a good parallelization of our code. For the NMMA framework, the parallelization is achieved by taking advantage of the flexibility of `dynesty`<sup>140</sup> and based on the interface presented in `parallelbilby`<sup>141</sup>.

In particular, the nested sampling process is parallelized using a head/worker strategy. The “head” organizes the live/dead points, and validates if the stopping criteria are reached, while the “workers” find new live points under the likelihood constraint. The theoretical scaling performance of such a strategy is given by<sup>142</sup>

$$T(N_{\text{cores}}) = T(N_{\text{core,ref}}) \times \frac{\ln(1 + N_{\text{core,ref}}/n_{\text{live}})}{\ln(1 + N_{\text{cores}}/n_{\text{live}})}, \quad (34)$$

where  $T(N_{\text{cores}})$  is the runtime using  $N_{\text{cores}}$  cores and  $T(N_{\text{core,ref}})$  is the reference time using  $N_{\text{core,ref}}$  cores. The parameter  $n_{\text{live}}$  denotes the number of live points.

To validate if such a scaling is achieved, we performed intensive scaling tests on SuperMUC\_NG at the Leibniz Supercomputing Centre (Munich), Lise and Emmy of the North German Supercomputing Alliance, and on HAWK of the High-Performance Computing Center Stuttgart. We show results for scaling tests performed on HAWK using AMD EPYC 7742 processors. The tests are based on a full joint inference of GW170817 & AT2017gfo and GW170817 & GRB170817A & AT2017gfo which includes intermediate checkpointing and all necessary I/O-operations. The strong scaling for such simulations is shown in Fig. 5 and is compared to the theoretical scaling mentioned of Eq. (34).

- Abbott, B. P. *et al.* Multi-messenger Observations of a Binary Neutron Star Merger. *Astrophys. J. Lett.* **848**, L12 (2017). 1710.05833.
- Abbott, B. P. *et al.* GW170817: Observation of Gravitational Waves from a Binary Neutron Star Inspiral. *Phys. Rev. Lett.* **119**, 161101 (2017). 1710.05832.
- Aasi, J. *et al.* Advanced LIGO. *Class. Quant. Grav.* **32**, 074001 (2015). 1411.4547.
- Acernese, F. *et al.* Advanced Virgo: a second-generation interferometric gravitational wave detector. *Class. Quant. Grav.* **32**, 024001 (2015). 1408.3978.
- Ajello, M. *et al.* Fermi-LAT Observations of High-Energy  $\gamma$ -Ray Emission Toward the Galactic Center. *Astrophys. J.* **819**, 44 (2016). 1511.02938.
- Winkler, C., Diehl, R., Ubertini, P. & Wilms, J. INTEGRAL: Science Highlights and Future Prospects. *Space Science Reviews* **161**, 149–177 (2011). 1110.6279.
- Metzger, B. D. Kilonovae. *Living Rev. Rel.* **23**, 1 (2020). 1910.01617.
- Coulter, D. A. *et al.* Swope Supernova Survey 2017a (SSS17a), the Optical Counterpart to a Gravitational Wave Source. *Science* (2017). [Science358,1556(2017)], 1710.05452.
- Bauswein, A., Just, O., Janka, H.-T. & Stergioulas, N. Neutron-star radius constraints from GW170817 and future detections. *Astrophys. J.* **850**, L34 (2017). 1710.06843.
- Ruiz, M., Shapiro, S. L. & Tsokaros, A. GW170817, General Relativistic Magnetohydrodynamic Simulations, and the Neutron Star Maximum Mass. *Phys. Rev.* **D97**, 021501 (2018). 1711.00473.
- Radice, D., Perego, A., Zappa, F. & Bernuzzi, S. GW170817: Joint Constraint on the Neutron Star Equation of State from Multimessenger Observations. *Astrophys. J.* **852**, L29 (2018). 1711.03647.
- Most, E. R., Weih, L. R., Rezzolla, L. & Schaffner-Bielich, J. New constraints on radii and tidal deformabilities of neutron stars from GW170817. *Phys. Rev. Lett.* **120**, 261103 (2018). 1803.00549.

13. Coughlin, M. W., Dietrich, T., Margalit, B. & Metzger, B. D. Multimessenger Bayesian parameter inference of a binary neutron star merger. *Monthly Notices of the Royal Astronomical Society: Letters* **489**, L91–L96 (2019). 1812.04803.
14. Capano, C. D. *et al.* Stringent constraints on neutron-star radii from multimessenger observations and nuclear theory. *Nature Astronomy* (2019). 1908.10352.
15. Dietrich, T. *et al.* Multimessenger constraints on the neutron-star equation of state and the Hubble constant. *Science* **370**, 1450–1453 (2020). 2002.11355.
16. Huth, S. *et al.* Constraining Neutron-Star Matter with Microscopic and Macroscopic Collisions. *arXiv:2107.06229* (2021).
17. Abbott, B. P. *et al.* A gravitational-wave standard siren measurement of the Hubble constant. *Nature*, 10.1038/nature24471 (2017). 1710.05835.
18. Guidorzi, C. *et al.* Improved Constraints on  $H_0$  from a Combined Analysis of Gravitational-wave and Electromagnetic Emission from GW170817. *Astrophys. J.* **851**, L36 (2017). 1710.06426.
19. Hotokezaka, K. *et al.* A Hubble constant measurement from superluminal motion of the jet in GW170817. *Nature Astron.* (2019). 1806.10596.
20. Coughlin, M. W. *et al.* On standardizing kilonovae and their use as standard candles to measure the Hubble constant. *Phys. Rev. Research*. **2**, 022006 (2020). 1908.00889.
21. Wang, H. & Giannios, D. Multimessenger parameter estimation of GW170817: from jet structure to the Hubble constant. *Astrophys. J.* **908**, 200 (2021). 2009.04427.
22. Abbott, B. *et al.* Multi-messenger Observations of a Binary Neutron Star Merger. *Astrophys. J. Lett.* **848**, L12 (2017). 1710.05833.
23. Breschi, M. *et al.* AT2017gfo: Bayesian inference and model selection of multicomponent kilonovae and constraints on the neutron star equation of state. *Mon. Not. Roy. Astron. Soc.* **505**, 1661–1677 (2021). 2101.01201.
24. Nicholl, M. *et al.* Tight multimessenger constraints on the neutron star equation of state from GW170817 and a forward model for kilonova light-curve synthesis. *Mon. Not. Roy. Astron. Soc.* **505**, 3016–3032 (2021). 2102.02229.
25. Raaijmakers, G. *et al.* The Challenges Ahead for Multimessenger Analyses of Gravitational Waves and Kilonova: A Case Study on GW190425. *Astrophys. J.* **922**, 269 (2021). 2102.11569.
26. Pang, P. T. H. *et al.* Nuclear Physics Multimessenger Astrophysics Constraints on the Neutron Star Equation of State: Adding NICER’s PSR J0740+6620 Measurement. *Astrophys. J.* **922**, 14 (2021). 2105.08688.
27. Tews, I. *et al.* On the Nature of GW190814 and Its Impact on the Understanding of Supranuclear Matter. *Astrophys. J. Lett.* **908**, L1 (2021). 2007.06057.
28. Andreoni, I. *et al.* Fast-transient Searches in Real Time with ZTFreST: Identification of Three Optically Discovered Gamma-Ray Burst Afterglows and New Constraints on the Kilonova Rate. *Astrophys. J.* **918**, 63 (2021). 2104.06352.
29. Ahumada, T. *et al.* Discovery and confirmation of the shortest gamma-ray burst from a collapsar. *Nature Astron.* **5**, 917–927 (2021). 2105.05067.
30. Tews, I., Carlson, J., Gandolfi, S. & Reddy, S. Constraining the speed of sound inside neutron stars with chiral effective field theory interactions and observations. *Astrophys. J.* **860**, 149 (2018). 1801.01923.
31. Tews, I., Margueron, J. & Reddy, S. Critical examination of constraints on the equation of state of dense matter obtained from GW170817. *Phys. Rev.* **C98**, 045804 (2018). 1804.02783.
32. Lynn, J. E. *et al.* Chiral Three-Nucleon Interactions in Light Nuclei, Neutron- $\alpha$  Scattering, and Neutron Matter. *Phys. Rev. Lett.* **116**, 062501 (2016). 1509.03470.
33. Holt, J. W. & Kaiser, N. Equation of state of nuclear and neutron matter at third-order in perturbation theory from chiral effective field theory. *Phys. Rev.* **C95**, 034326 (2017). 1612.04309.
34. Drischler, C., Hebeler, K. & Schwenk, A. Chiral interactions up to next-to-next-to-next-to-leading order and nuclear saturation. *Phys. Rev. Lett.* **122**, 042501 (2019). 1710.08220.
35. Piarulli, M., Bombaci, I., Logoteta, D., Lovato, A. & Wiringa, R. B. Benchmark calculations of pure neutron matter with realistic nucleon-nucleon interactions. *Phys. Rev. C* **101**, 045801 (2020). 1908.04426.
36. Keller, J., Wellenhofer, C., Hebeler, K. & Schwenk, A. Neutron matter at finite temperature based on chiral effective field theory interactions. *Phys. Rev. C* **103**, 055806 (2021). 2011.05855.
37. Russotto, P. *et al.* Results of the ASY-EOS experiment at GSI: The symmetry energy at suprasaturation density. *Phys. Rev. C* **94**, 034608 (2016). 1608.04332.
38. Adhikari, D. *et al.* Accurate Determination of the Neutron Skin Thickness of  $^{208}\text{Pb}$  through Parity-Violation in Electron Scattering. *Phys. Rev. Lett.* **126**, 172502 (2021). 2102.10767.
39. Antoniadis, J. *et al.* A Massive Pulsar in a Compact Relativistic Binary. *Science* **340**, 6131 (2013). 1304.6875.
40. Arzoumanian, Z. *et al.* The NANOGrav 11-year Data Set: High-precision timing of 45 Millisecond Pulsars. *Astrophys. J. Suppl.* **235**, 37 (2018). 1801.01837.
41. Cromartie, H. T. *et al.* Relativistic Shapiro delay measurements of an extremely massive millisecond pulsar. *Nature Astron.* **4**, 72–76 (2019). 1904.06759.
42. Kurkela, A., Fraga, E. S., Schaffner-Bielich, J. & Vuorinen, A. Constraining neutron star matter with Quantum Chromodynamics. *Astrophys. J.* **789**, 127 (2014). 1402.6618.
43. Komoltsev, O. & Kurkela, A. How perturbative QCD constrains the Equation of State at Neutron-Star densities. *arXiv:2111.05350* (2021).
44. Vallisneri, M. Use and abuse of the Fisher information matrix in the assessment of gravitational-wave parameter-estimation prospects. *Phys. Rev.* **D77**, 042001 (2008). gr-qc/0703086.
45. Abbott, B. P. *et al.* Properties of the binary neutron star merger GW170817. *Phys. Rev.* **X9**, 011001 (2019). 1805.11579.
46. Heinzel, J. *et al.* Comparing inclination dependent analyses of kilonova transients. *Mon. Not. Roy. Astron. Soc.* **502**, 3057–3065 (2021). 2010.10746.
47. Siegel, D. M. GW170817—the first observed neutron star merger and its kilonova: implications for the astrophysical site of the r-process. *Eur. Phys. J. A* **55**, 203 (2019). 1901.09044.
48. Radice, D. *et al.* Binary Neutron Star Mergers: Mass Ejection, Electromagnetic Counterparts and Nucleosynthesis. *Astrophys. J.* **869**, 130 (2018). 1809.11161.
49. van Eerten, H., Zhang, W. & MacFadyen, A. Off-Axis Gamma-Ray Burst Afterglow Modeling Based On A Two-Dimensional Axisymmetric Hydrodynamics Simulation. *Astrophys. J.* **722**, 235–247 (2010). 1006.5125.
50. Ryan, G., van Eerten, H., Piro, L. & Troja, E. Gamma-Ray Burst Afterglows in the Multimessenger Era: Numerical Models and Closure Relations. *Astrophys. J.* **896**, 166 (2020). 1909.11691.
51. Essick, R., Tews, I., Landry, P., Reddy, S. & Holz, D. E. Direct Astrophysical Tests of Chiral Effective Field Theory at Supranuclear Densities. *arxiv:2004.07744* (2020).
52. Miller, M. C. *et al.* The Radius of PSR J0740+6620 from NICER and XMM-Newton Data. *Astrophys. J. Lett.* **918**, L28 (2021). 2105.06979.
53. URL <https://github.com/nuclear-multimessenger-astronomy>.
54. Baym, G., Pethick, C. & Sutherland, P. The Ground State of Matter at High Densities: Equation of State and Stellar Models. *Astrophys. J.* **170**, 299+ (1971).
55. Tews, I. *et al.* Nuclear Forces for Precision Nuclear Physics – a collection of perspectives. *arXiv* (2022). 2202.01105.
56. Krüger, T., Tews, I., Hebeler, K. & Schwenk, A. Neutron matter from chiral effective field theory interactions. *Phys. Rev. C* **88**, 025802 (2013). 1304.2212.
57. Epelbaum, E., Hammer, H.-W. & Meißner, U.-G. Modern Theory of Nuclear Forces. *Rev. Mod. Phys.* **81**, 1773–1825 (2009). 0811.1338.
58. Machleidt, R. & Entem, D. R. Chiral effective field theory and nuclear forces. *Phys. Rept.* **503**, 1–75 (2011). 1105.2919.
59. Drischler, C., Melendez, J. A., Furnstahl, R. J. & Phillips, D. R. Quantifying uncertainties and correlations in the nuclear-matter equation of state. *Phys. Rev. C* **102**, 054315 (2020). 2004.07805.
60. Weinberg, S. Nuclear forces from chiral Lagrangians. *Phys. Lett. B* **251**, 288–292 (1990).
61. Weinberg, S. Effective chiral Lagrangians for nucleon - pion interactions and nuclear forces. *Nucl. Phys. B* **363**, 3–18 (1991).
62. Weinberg, S. Three body interactions among nucleons and pions. *Phys. Lett. B* **295**, 114–121 (1992). hep-ph/9209257.
63. Epelbaum, E., Krebs, H. & Meißner, U.-G. Improved chiral nucleon-nucleon potential up to next-to-next-to-next-to-leading order. *Eur. Phys. J. A* **51**, 53 (2015). URL <http://dx.doi.org/10.1140/epja/i2015-15053-8>. 1412.0142.
64. Drischler, C., Furnstahl, R. J., Melendez, J. A. & Phillips, D. R. How Well Do We Know the Neutron-Matter Equation of State at the Densities Inside Neutron Stars? A Bayesian Approach with Correlated Uncertainties. *Phys. Rev. Lett.* **125**, 202702 (2020). 2004.07232.
65. Ekström, A., Hagen, G., Morris, T. D., Papenbrock, T. & Schwartz, P. D.  $\Delta$  isobars and nuclear saturation. *Phys. Rev. C* **97**, 024332 (2018). 1707.09028.
66. Tews, I., Krüger, T., Hebeler, K. & Schwenk, A. Neutron matter at next-to-next-to-next-to-leading order in chiral effective field theory. *Phys. Rev. Lett.* **110**, 032504 (2013). 1206.0025.

67. Carbone, A., Cipollone, A., Barbieri, C., Rios, A. & Polls, A. Self-consistent Green's functions formalism with three-body interactions. *Phys. Rev. C* **88**, 054326 (2013). 1310.3688.
68. Hagen, G. *et al.* Coupled-cluster calculations of nucleonic matter. *Phys. Rev. C* **89**, 014319 (2014). 1311.2925.
69. Carlson, J. *et al.* Quantum Monte Carlo methods for nuclear physics. *Rev. Mod. Phys.* **87**, 1067 (2015).
70. Schmidt, K. E. & Fantoni, S. A quantum Monte Carlo method for nucleon systems. *Phys. Lett. B* **446**, 99–103 (1999).
71. Read, J. S., Lackey, B. D., Owen, B. J. & Friedman, J. L. Constraints on a phenomenologically parameterized neutron-star equation of state. *Phys. Rev. D* **79**, 124032 (2009). 0812.2163.
72. Hebeler, K., Lattimer, J., Pethick, C. & Schwenk, A. Equation of state and neutron star properties constrained by nuclear physics and observation. *Astrophys. J.* **773**, 11 (2013). 1303.4662.
73. Annala, E., Gorda, T., Kurkela, A. & Vuorinen, A. Gravitational-wave constraints on the neutron-star-matter Equation of State. *Phys. Rev. Lett.* **120**, 172703 (2018). 1711.02644.
74. Tews, I., Margueron, J. & Reddy, S. Critical examination of constraints on the equation of state of dense matter obtained from GW170817. *Phys. Rev. C* **98**, 045804 (2018). 1804.02783.
75. Greif, S., Raaijmakers, G., Hebeler, K., Schwenk, A. & Watts, A. Equation of state sensitivities when inferring neutron star and dense matter properties. *Mon. Not. Roy. Astron. Soc.* **485**, 5363–5376 (2019). 1812.08188.
76. Essick, R., Landry, P. & Holz, D. E. Nonparametric Inference of Neutron Star Composition, Equation of State, and Maximum Mass with GW170817. *Phys. Rev. D* **101**, 063007 (2020). 1910.09740.
77. McLerran, L. & Reddy, S. Quarkyonic Matter and Neutron Stars. *Phys. Rev. Lett.* **122**, 122701 (2019). 1811.12503.
78. Jeong, K. S., McLerran, L. & Sen, S. Dynamically generated momentum space shell structure of quarkyonic matter via an excluded volume model. *Phys. Rev. C* **101**, 035201 (2020). 1908.04799.
79. Sen, S. & Sivertsen, L. Mass and Radius Relations of Quarkyonic Stars Using an Excluded-volume Model. *Astrophys. J.* **915**, 109 (2021). 2011.04681.
80. Margueron, J., Hansen, H., Proust, P. & Chanfray, G. Quarkyonic stars with isospin-flavor asymmetry. *Phys. Rev. C* **104**, 055803 (2021). 2103.10209.
81. Gandolfi, S., Carlson, J. & Reddy, S. The maximum mass and radius of neutron stars and the nuclear symmetry energy. *Phys. Rev. C* **85**, 032801 (2012). 1101.1921.
82. Wolff, M. T. *et al.* NICER Detection of Thermal X-Ray Pulsations from the Massive Millisecond Pulsars PSR J0740+6620 and PSR J1614–2230. *Astrophys. J. Lett.* **918**, L26 (2021). 2105.06978.
83. Miller, M. C. *et al.* PSR J0030+0451 Mass and Radius from NICER Data and Implications for the Properties of Neutron Star Matter. *Astrophys. J. Lett.* **887**, L24 (2019). 1912.05705.
84. Riley, T. E. *et al.* A NICER View of PSR J0030+0451: Millisecond Pulsar Parameter Estimation. *Astrophys. J. Lett.* **887**, L21 (2019). 1912.05702.
85. Riley, T. E. *et al.* A NICER View of the Massive Pulsar PSR J0740+6620 Informed by Radio Timing and XMM-Newton Spectroscopy. *Astrophys. J. Lett.* **918**, L27 (2021). 2105.06980.
86. Damour, T. & Nagar, A. Relativistic tidal properties of neutron stars. *Phys. Rev. D* **80**, 084035 (2009). 0906.0096.
87. Hinderer, T., Lackey, B. D., Lang, R. N. & Read, J. S. Tidal deformability of neutron stars with realistic equations of state and their gravitational wave signatures in binary inspiral. *Phys. Rev. D* **81**, 123016 (2010). 0911.3535.
88. Abbott, B. P. *et al.* GW170817: Measurements of neutron star radii and equation of state. *Phys. Rev. Lett.* **121**, 161101 (2018). 1805.11581.
89. Abbott, B. P. *et al.* Model comparison from LIGO–Virgo data on GW170817's binary components and consequences for the merger remnant. *Class. Quant. Grav.* **37**, 045006 (2020). 1908.01012.
90. Carney, M. F., Wade, L. E. & Irwin, B. S. Comparing two models for measuring the neutron star equation of state from gravitational-wave signals. *Phys. Rev. D* **98**, 063004 (2018). 1805.11217.
91. Damour, T., Nagar, A. & Villain, L. Measurability of the tidal polarizability of neutron stars in late-inspiral gravitational-wave signals. *Phys. Rev. D* **85**, 123007 (2012). 1203.4352.
92. Abdelsalhin, T., Gualtieri, L. & Pani, P. Post-Newtonian spin-tidal couplings for compact binaries. *arXiv:1805.01487* (2018).
93. Landry, P. Rotational-tidal phasing of the binary neutron star waveform. *arXiv:1805.01882* (2018).
94. Jiménez Forteza, X., Abdelsalhin, T., Pani, P. & Gualtieri, L. Impact of high-order tidal terms on binary neutron-star waveforms. *Phys. Rev. D* **98**, 124014 (2018). 1807.08016.
95. Buonanno, A. & Damour, T. Effective one-body approach to general relativistic two-body dynamics. *Phys. Rev. D* **59**, 084006 (1999). gr-qc/9811091.
96. Damour, T. & Nagar, A. Effective One Body description of tidal effects in inspiralling compact binaries. *Phys. Rev. D* **81**, 084016 (2010). 0911.5041.
97. Hotokezaka, K., Kyutoku, K., Okawa, H. & Shibata, M. Exploring tidal effects of coalescing binary neutron stars in numerical relativity. II. Long-term simulations. *Phys. Rev. D* **91**, 064060 (2015). 1502.03457.
98. Hinderer, T. *et al.* Effects of neutron-star dynamic tides on gravitational waveforms within the effective-one-body approach. *Phys. Rev. Lett.* **116**, 181101 (2016). 1602.00599.
99. Akcay, S. *et al.* Effective-one-body multipolar waveform for tidally interacting binary neutron stars up to merger. *Phys. Rev. D* **99**, 044051 (2019). 1812.02744.
100. Bernuzzi, S., Nagar, A., Dietrich, T. & Damour, T. Modeling the Dynamics of Tidally Interacting Binary Neutron Stars up to the Merger. *Phys. Rev. Lett.* **114**, 161103 (2015). 1412.4553.
101. Dietrich, T. & Hinderer, T. Comprehensive comparison of numerical relativity and effective-one-body results to inform improvements in waveform models for binary neutron star systems. *Phys. Rev. D* **95**, 124006 (2017). 1702.02053.
102. Nagar, A. *et al.* Time-domain effective-one-body gravitational waveforms for coalescing compact binaries with nonprecessing spins, tides and self-spin effects. *Phys. Rev. D* **98**, 104052 (2018). 1806.01772.
103. Steinhoff, J., Hinderer, T., Dietrich, T. & Foucart, F. Spin effects on neutron star fundamental-mode dynamical tides: Phenomenology and comparison to numerical simulations. *Phys. Rev. Res.* **3**, 033129 (2021). 2103.06100.
104. Kawaguchi, K. *et al.* Frequency-domain gravitational waveform models for inspiraling binary neutron stars. *Phys. Rev. D* **97**, 044044 (2018). 1802.06518.
105. Dietrich, T., Bernuzzi, S. & Tichy, W. Closed-form tidal approximants for binary neutron star gravitational waveforms constructed from high-resolution numerical relativity simulations. *Phys. Rev. D* **96**, 121501 (2017). 1706.02969.
106. Dietrich, T. *et al.* Matter imprints in waveform models for neutron star binaries: Tidal and self-spin effects. *Phys. Rev. D* **99**, 024029 (2019). 1804.02235.
107. Dietrich, T. *et al.* Improving the NRTidal model for binary neutron star systems. *Phys. Rev. D* **100**, 044003 (2019). 1905.06011.
108. Thompson, J. E. *et al.* Modeling the gravitational wave signature of neutron star black hole coalescences. *Phys. Rev. D* **101**, 124059 (2020). 2002.08383.
109. LIGO Scientific Collaboration. LIGO Algorithm Library - LALSuite. free software (GPL) (2018).
110. Steinhoff, J., Hinderer, T., Buonanno, A. & Taracchini, A. Dynamical Tides in General Relativity: Effective Action and Effective-One-Body Hamiltonian. *Phys. Rev. D* **94**, 104028 (2016). 1608.01907.
111. Lackey, B. D., Pürer, M., Taracchini, A. & Marsat, S. Surrogate model for an aligned-spin effective one body waveform model of binary neutron star inspirals using Gaussian process regression. *Phys. Rev. D* **100**, 024002 (2019). 1812.08643.
112. Nagar, A. *et al.* Nonlinear-in-spin effects in effective-one-body waveform models of spin-aligned, inspiralling, neutron star binaries. *Phys. Rev. D* **99**, 044007 (2019). 1812.07923.
113. Nagar, A. & Rettegno, P. Efficient effective one body time-domain gravitational waveforms. *Phys. Rev. D* **99**, 021501 (2019). 1805.03891.
114. Matas, A. *et al.* Aligned-spin neutron-star–black-hole waveform model based on the effective-one-body approach and numerical-relativity simulations. *Phys. Rev. D* **102**, 043023 (2020). 2004.10001.
115. Veitch, J. *et al.* Parameter estimation for compact binaries with ground-based gravitational-wave observations using the LALInference software library. *Phys. Rev. D* **91**, 042003 (2015). 1409.7215.
116. Bulla, M. POSSIS: predicting spectra, light curves and polarization for multi-dimensional models of supernovae and kilonovae. *Mon. Not. Roy. Astron. Soc.* **489**, 5037–5045 (2019). 1906.04205.
117. Mazzali, P. A. & Lucy, L. B. The Application of Monte Carlo methods to the synthesis of early-time supernovae spectra. *Astron. Astrophys.* **279**, 447 (1993).
118. Magee, M. R., Sim, S. A., Kotak, R. & Kerzendorf, W. E. Modelling the early time behaviour of type Ia supernovae: effects of the  $^{56}\text{Ni}$  distribution. *Astron. Astrophys.* **614**, A115 (2018). 1803.04436.
119. Tanaka, M., Kato, D., Gaigalas, G. & Kawaguchi, K. Systematic opacity calculations for kilonovae. *Monthly Notices of the Royal Astronomical Society* **496**, 1369–1392 (2020). 1906.08914.

120. Bulla, M., Sim, S. A. & Kromer, M. Polarization spectral synthesis for Type Ia supernova explosion models. *Monthly Notices of the Royal Astronomical Society* **450**, 967–981 (2015). 1503.07002.
121. Barbary, K. *et al.* Sncosmo (2022). URL <https://doi.org/10.5281/zenodo.6363879>. If you use Sncosmo, please cite it using these metadata.
122. Coughlin, M. *et al.* Toward Rapid Transient Identification and Characterization of Kilonovae. *Astrophys. J.* **849**, 12 (2017). 1708.07714.
123. Sari, R., Piran, T. & Narayan, R. Spectra and light curves of gamma-ray burst afterglows. *Astrophys. J. Lett.* **497**, L17 (1998). astro-ph/9712005.
124. Eichler, D., Livio, M., Piran, T. & Schramm, D. N. Nucleosynthesis, Neutrino Bursts and Gamma-Rays from Coalescing Neutron Stars. *Nature* **340**, 126–128 (1989).
125. Paczynski, B. Cosmological gamma-ray bursts. *Acta Astron.* **41**, 257–267 (1991).
126. Meszaros, P. & Rees, M. J. Tidal heating and mass loss in neutron star binaries - Implications for gamma-ray burst models. *Astrophys. J.* **397**, 570–575 (1992).
127. Narayan, R., Paczynski, B. & Piran, T. Gamma-ray bursts as the death throes of massive binary stars. *Astrophys. J.* **395**, L83–L86 (1992). astro-ph/9204001.
128. van Eerten, H., Leventis, K., Meliani, Z., Wijers, R. & Keppens, R. Gamma-ray burst afterglows from trans-relativistic blast wave simulations. *Mon. Not. Roy. Astron. Soc.* **403**, 300 (2010). 0909.2446.
129. Granot, J. & Piran, T. On the lateral expansion of gamma-ray burst jets. *Monthly Notices of the Royal Astronomical Society* **421**, 570–587 (2012). URL <https://doi.org/10.1111/j.1365-2966.2011.20335.x>. astro-ph/1109.6468.
130. Krüger, C. J. & Foucart, F. Estimates for Disk and Ejecta Masses Produced in Compact Binary Mergers. *Phys. Rev. D* **101**, 103002 (2020). 2002.07728.
131. Dietrich, T. & Ujevic, M. Modeling dynamical ejecta from binary neutron star mergers and implications for electromagnetic counterparts. *Class. Quant. Grav.* **34**, 105014 (2017). 1612.03665.
132. Coughlin, M. W. *et al.* Constraints on the neutron star equation of state from at2017gfo using radiative transfer simulations. *Monthly Notices of the Royal Astronomical Society* **480**, 3871–3878 (2018). 1805.09371.
133. Nedora, V. *et al.* Mapping dynamical ejecta and disk masses from numerical relativity simulations of neutron star mergers. *Class. Quant. Grav.* **39**, 015008 (2022). 2011.11110.
134. Agathos, M. *et al.* Inferring Prompt Black-Hole Formation in Neutron Star Mergers from Gravitational-Wave Data. *Phys. Rev. D* **101**, 044006 (2020). 1908.05442.
135. Rasmussen, C. E. & Williams, C. K. I. *Gaussian Processes for Machine Learning* (MIT Press, 2006).
136. Pedregosa, F. *et al.* Scikit-learn: Machine learning in Python. *Journal of Machine Learning Research* **12**, 2825–2830 (2011).
137. Almualla, M. *et al.* Using Neural Networks to Perform Rapid High-Dimensional Kilonova Parameter Inference. *arXiv:2112.15470* (2021).
138. Abadi, M. *et al.* TensorFlow: Large-scale machine learning on heterogeneous systems (2015). URL <https://www.tensorflow.org/>. Software available from tensorflow.org.
139. Kunert, N., Pang, P. T. H., Tews, I., Coughlin, M. W. & Dietrich, T. Quantifying modeling uncertainties when combining multiple gravitational-wave detections from binary neutron star sources. *Phys. Rev. D* **105**, L061301 (2022). 2110.11835.
140. Speagle, J. S. dynesty: a dynamic nested sampling package for estimating Bayesian posteriors and evidences. *Mon. Not. Roy. Astron. Soc.* **493**, 3132–3158 (2020). 1904.02180.
141. Smith, R. J. E., Ashton, G., Vajpeyi, A. & Talbot, C. Massively parallel Bayesian inference for transient gravitational-wave astronomy. *Mon. Not. Roy. Astron. Soc.* **498**, 4492–4502 (2020). 1909.11873.
142. Handley, W., Hobson, M. & Lasenby, A. PolyChord: nested sampling for cosmology. *Mon. Not. Roy. Astron. Soc.* **450**, L61–L65 (2015). 1502.01856.
143. Pang, P. T. H. *et al.* NMMA: A nuclear-physics and multi-messenger astrophysics framework to analyze binary neutron star mergers (2022). URL <https://doi.org/10.5281/zenodo.6551053>.

## 6 Data Availability

The posterior samples for the primary analyses are available in the data release<sup>143</sup>.

## 7 Code Availability

The program for the study is publicly available<sup>53</sup>.

## 8 Acknowledgements

We thank N. Andersson, R. Essick, P. Landry, and J. Margueron for insightful discussions. P.T.H.P and C.V.D.B. are supported by the research program of the Netherlands Organization for Scientific Research (NWO). M.W.C. acknowledges support from the National Science Foundation with grant numbers PHY-2010970 and OAC-2117997. M.B. acknowledges support from the Swedish Research Council (Reg. no. 2020-03330). The work of I.T. was supported by the U.S. Department of Energy, Office of Science, Office of Nuclear Physics, under contract No. DE-AC52-06NA25396, by the Laboratory Directed Research and Development program of Los Alamos National Laboratory under project number 20220658ER, and by the U.S. Department of Energy, Office of Science, Office of Advanced Scientific Computing Research, Scientific Discovery through Advanced Computing (SciDAC) program. J.H. acknowledges support from the National Science Foundation with grant number PHY-1806990.

Computations have been performed on the Minerva HPC cluster of the Max-Planck-Institute for Gravitational Physics and on SuperMUC-NG (LRZ) under project number pn56zo. Computational resources have also been provided by the Los Alamos National Laboratory Institutional Computing Program, which is supported by the U.S. Department of Energy National Nuclear Security Administration under Contract No. 89233218CNA000001, and by the National Energy Research Scientific Computing Center (NERSC), which is supported by the U.S. Department of Energy, Office of Science, under contract No. DE-AC02-05CH11231. Resources supporting this work were provided by the Minnesota Supercomputing Institute (MSI) at University of Minnesota under the project “Identification of Variable Objects in the Zwicky Transient Facility,” and the Supercomputing Laboratory at King Abdullah University of Science & Technology (KAUST) in Thuwal, Saudi Arabia. This research has made use of data, software and/or web tools obtained from the Gravitational Wave Open Science Center (<https://www.gw-openscience.org>), a service of LIGO Laboratory, the LIGO Scientific Collaboration and the Virgo Collaboration. This material is based upon work supported by NSF’s LIGO Laboratory which is a major facility fully funded by the National Science Foundation. Virgo is funded by the French Centre National de Recherche Scientifique (CNRS), the Italian Istituto Nazionale della Fisica Nucleare (INFN) and the Dutch Nikhef, with contributions by Polish and Hungarian institutes.

## 9 Author contributions

Conceptualisation: PTHP, TD, MC, MB, IT, CvdB;  
Methodology: PTHP, TD, MC, MB, IT, MA, SA, CvdB;  
Data curation: PTHP, MC, MA;  
Software: PTHP, TD, MC, MB, IT, MA, TB, WK, NK, GM, BR, NS, AT, SA, RV, JH, PS, RSh, RSo, CvdB;  
Validation: PTHP, MC;  
Formal analysis: PTHP, MC;  
Resources: TD, MC, MB, IT;  
Funding acquisition: TD, MWC, MB, IT;  
Project administration: PTHP, TD, MC, MB, IT, CvdB;  
Supervision: PTHP, TD, MC, MB, IT;  
Visualisation: PTHP, TD, MC, MB, IT, NK;  
Writing—original draft: PTHP, TD, MC, MB, IT, NK, VN, PS;

Writing—review and editing: PTHP, TD, MC, MB, IT, NK, VN.

## 10 Competing interests

The authors declare that they have no competing financial interests.

## 11 Correspondence

tim.dietrich@uni-potsdam.de